

Physics-based Full-band GaN HEMT Simulation Suggests Upper Bound of LO Phonon Lifetime

Ankan Ghosh Dastider,^{1,2} Matt Grupen,³ Ashwin Tunga,^{1,2} and Shaloo Rakheja^{*,1,2}

¹*Department of Electrical and Computer Engineering, University of Illinois Urbana-Champaign, Urbana, IL, USA*

²*Holonyak Micro and Nanotechnology Laboratory, University of Illinois Urbana-Champaign, Urbana, IL, USA*

³*Air Force Research Laboratory Sensors Directorate, 2241 Avionics Cir., Wright-Patterson AFB, OH, USA*

(*Electronic mail: rakheja@illinois.edu)

(Dated: 9 December 2025)

Intrinsic limits to device performance arise from fundamental material properties that define the best achievable operation, independent of engineering constraints. In GaN HEMTs, hot longitudinal optical (LO) phonons can act as an intrinsic performance bottleneck by reducing electron saturation velocity, output current, and transconductance—metrics that are important for device operation. While bulk GaN studies report LO phonon lifetimes of ~ 1 ps, leading to strong nonequilibrium phonon populations, ungated heterostructures show much shorter lifetimes of only tens of femtoseconds. Because direct measurement in HEMTs is challenging, the true impact of hot phonons remains uncertain. Full-band transport simulations of a fabricated GaN HEMT presented here reveal that LO phonon lifetimes must be $\lesssim 40$ fs to reproduce measured I–V characteristics, consistent with ultrafast decay observed in GaN heterostructures. We show that even this ultrafast LO-phonon decay is insufficient to fully suppress hot-phonon effects: the residual nonequilibrium LO population continues to limit the current density at high bias. Moreover, when the LO-phonon lifetime exceeds a few tens of femtoseconds, a pronounced hot-phonon bottleneck emerges, leading to a substantial current-density suppression that is inconsistent with experimental observations.

I. INTRODUCTION

GaN-based high-electron-mobility transistor (HEMT) is an attractive technology for high-frequency and high-power electronics needed in satellite communications, radar systems, and wireless communication networks.^{1,2} The exceptional material properties of GaN, including its wide bandgap, high breakdown voltage,³ and large peak electron velocity,⁴ enable devices to operate under high electric fields and deliver superior power densities. The strong spontaneous and piezoelectric polarizations in AlGaIn/GaN heterostructures give rise to a high-density two-dimensional electron gas (2DEG) at the interface without the need for modulation doping,⁵ an intrinsic feature that forms the basis for the excellent electrical behavior observed in GaN HEMTs.

Electron-phonon scatterings in a device often set intrinsic limits on device performance, independent of engineering or processing constraints. In the case of GaN, the optical phonon energy is high because of the light mass of the nitrogen atom, which combined with the high electronegativity of nitrogen, results in a high electron-LO phonon scattering rate.⁶ If a hot electron in GaN relaxes its energy by emitting an LO phonon that does not decay rapidly into acoustic modes, it could lead to the accumulation of hot LO phonons^{7–11} since the velocity of optical phonons is negligible.^{12,13} This accumulation of hot LO phonons could result in an intrinsic performance bottleneck of the GaN technology, necessitating innovations in heat extraction and phonon engineering. This paper’s central goal is to clearly answer the question of whether hot LO phonons are critical to the performance of a GaN HEMT and compare our predictions of hot LO phonon lifetimes to prior measurements in ungated GaN heterostructures.

Electron transport in a fabricated GaN HEMT is simulated

using our in-house deterministic full-band Boltzmann solver, Fermi Kinetics Transport (FKT),^{14–17} which explicitly captures LO phonon dynamics. Simulations compared to measured I–V characteristics confirm that, unlike bulk GaN where LO phonon lifetimes can be relatively long, the effective lifetime in GaN HEMTs is significantly shorter. This suppression of phonon lifetime is attributed to plasmon–phonon coupling and the influence of heterointerfaces inherent to HEMT structures.^{18,19} Additional simulations show that, even with ultrafast LO-phonon decay, the hot-phonon bottleneck in GaN HEMTs persists, leading to as much as 30–60% reduction in both saturation current and peak transconductance, reinforcing that LO phonons remain an intrinsic performance limiter. Moreover, LO-phonon lifetimes exceeding a few tens of femtoseconds produce phonon heating and I–V characteristics that deviate markedly from experimental measurements, indicating that such long lifetimes are not physically realistic for GaN HEMTs.

II. FERMI KINETICS TRANSPORT SOLVER

Our work is based on FKT, which solves the Boltzmann transport equation (BTE) in the deterministic sense, making it computationally more efficient than Monte Carlo solvers. Unlike other deterministic Boltzmann solvers, FKT uniquely handles electronic heat flow using the heat capacity of an ideal Fermi gas instead of relying on an arbitrarily defined electron thermal conductivity. This alternative closure relation enhances the numerical stability and convergence of FKT compared to traditional solvers.¹⁴ FKT employs the method of moments to compute both electron and energy fluxes and is capable of incorporating detailed electronic bandstruc-

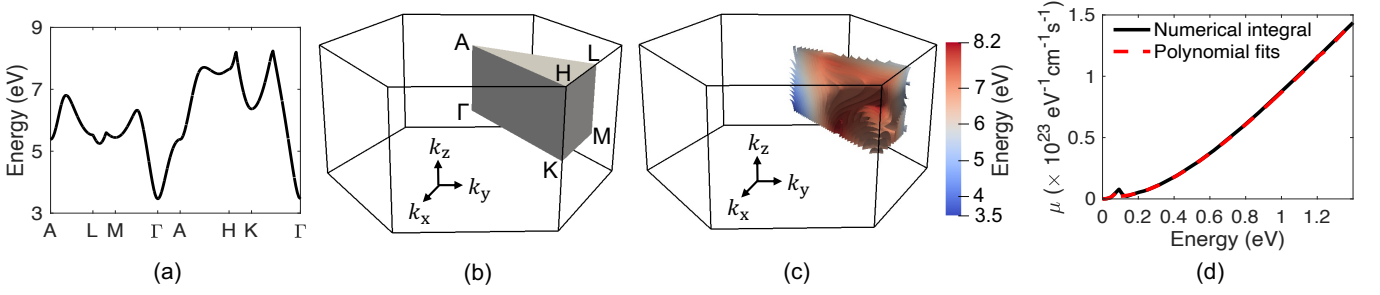


FIG. 1. Workflow for preprocessing transport quantities: from (a) EPM bandstructure, (b) Brillouin-zone computation, and (c) iso-surface extraction to (d) polynomial fitting of transport integrals used in FKT simulations.

tures and key scattering mechanisms based on Fermi's golden rule.¹⁵ It can also couple rapid hot electron dynamics with much slower defect ionization processes to simulate operational instabilities and with full wave electromagnetic fields to enable large signal RF simulations.²⁰ These features make FKT a versatile tool for advanced electron transport modeling.

A. Incorporating Electronic Band Structure and Scattering

Within the FKT framework, electron energy isosurfaces derived from the electronic band structure serve as the basis for precomputing all energy-dependent quantities needed for transport simulation in the device. This procedure is carried out in bulk GaN, prior to carrying out the transport simulations. The carrier density and electron particle flux are expressed in terms of isosurface integrals that depend on the electronic band structure and scattering mechanisms. For example, the carrier density is given by:

$$n_i = \int_{E_i} \left[\int_{\mathbf{k}_i} \underbrace{\frac{1}{4\pi^3} \frac{\delta(E_{\mathbf{k}} - E)}{|\nabla_{\mathbf{k}} E|}}_{\rho_{\mathbf{k}}(E)} d\mathbf{k} \right] f_i(E) dE, \quad (1)$$

where $f_i(E)$ is the Fermi-Dirac distribution function assigned to the i -th local carrier population, and the term in square brackets is the density of electron states $\rho_{\mathbf{k}}(E)$ integrated over all degenerate momentum vectors associated with the local distribution function $f_i(E)$. Since multiple Fermi-Dirac distributions are assigned to a given point in real space, the total density is obtained by summing the contributions. From the first moment of the BTE, the particle flux is given by an integral of the form:

$$J_i = \int_{E_i} \underbrace{\left[\int_{\mathbf{k}_i} \mathbf{v} \mathbf{v}^T \tau_{\mathbf{k}} \rho_{\mathbf{k}}(E) d\mathbf{k} \right]}_{\mu} \left(qE \frac{\partial f_i}{\partial E} - \nabla f_i \right) dE, \quad (2)$$

where electron velocity $\mathbf{v} = \nabla_{\mathbf{k}} E / \hbar$, and $\tau_{\mathbf{k}}(E)$ is the momentum relaxation time contributed by all scattering mechanisms, while μ represents the energy isosurface integral.¹⁶

The overview of the entire preprocessing stage is illustrated in Fig. 1. An empirical pseudopotential method (EPM)-computed band structure,²¹ shown in Fig. 1(a), is employed

for wurtzite GaN, and the irreducible wedge of its first Brillouin zone, shown in Fig. 1(b), is filled with a conformal tetrahedral mesh to determine the electron energies at discrete \mathbf{k} -points. Using piecewise-linear interpolation along the mesh edges, the electron energy isosurfaces are extracted¹⁵ as shown in Fig. 1(c). The integral μ in Eq. (2) is computed over each energy isosurface to produce an energy spectrum like that shown in Fig. 1(d). Because lattice temperature, LO phonon temperature, ionized defect density, and electron density vary sensitively during device operation, the flux isosurface integrals must evolve correspondingly. In order to capture the dependence of these four quantities, the computed integrals are first fitted to polynomials of electron energy, and the resulting polynomial coefficients are subsequently parameterized as functions of the four varying quantities, *i.e.*, lattice temperature, LO phonon temperature, ionized defect density, and electron density. Therefore, the simulator is capable of using these four changing quantities to obtain the correct flux isosurface integrals matching the actual numerical integrals.

Figure 2 highlights the necessity to explicitly consider LO phonon temperature in the solver. This figure plots the Γ valley isosurface integrals when the LO phonon temperature is varied while the other parameters (lattice temperature, ionized defect density, and electron density) are held constant. The energy isosurface integral increases with energy up to approximately 92 meV, driven by the growth of the velocity vector \mathbf{v} and the density of states $\rho_{\mathbf{k}}(E)$, even though $\tau_{\mathbf{k}}(E)$ itself begins to decline. At around 92 meV, when electrons begin to emit optical phonons in addition to absorbing them, $\tau_{\mathbf{k}}(E)$ decreases sharply, leading to a reduction in the overall integral. At higher energies, the integrals gradually rise again. With increasing LO phonon temperature, the phonon occupation number rises, enhancing both absorption and emission scattering rates. Consequently, $\tau_{\mathbf{k}}(E)$ decreases across all electron energies, leading to a uniform reduction in the flux isosurface integrals throughout the spectrum.

B. Treatment of Acoustic and Optical Phonons

In the quasi-static setup employed here, the rotational electric and magnetic fields are ignored, while FKT self-consistently solves Poisson's equation, mobile electron particle and energy continuity, as well as the conservation of lattice

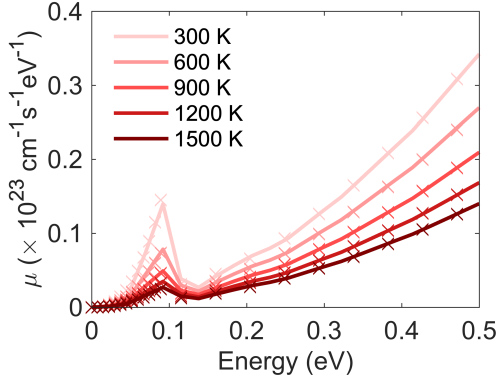


FIG. 2. Γ valley flux isosurface integrals in the horizontal plane of GaN with varying LO phonon temperatures at 300 K lattice temperature and 10^{18} cm^{-3} ionized defect and mobile electron densities.

energy. The lattice energy conservation is given as

$$\rho C_p \frac{\partial T_A}{\partial t} + \nabla \cdot \kappa \nabla T_A - C^E = 0, \quad (3)$$

where T_A is the acoustic phonon (lattice) temperature, C_p is the specific heat capacity, κ is the effective thermal conductivity (determined by the longitudinal acoustic (LA) and transverse acoustic (TA) modes in GaN), and C^E is the energy collision operator. When hot LO phonons are considered, C^E is replaced with the LO phonon's decay rate times its energy $\hbar\omega_{LO}$.

Under high electric fields, the generation of LO phonons increases, which also increases the electron momentum relaxation rate due to the electron-LO scattering events. The finite lifetime of LO phonons (τ_{LO}) results in a non-equilibrium population of LO phonons, also termed as hot phonons. The distribution of LO phonons is given by the following mode rate equation:

$$\frac{1}{8\pi^3} \int d\mathbf{q} \frac{dn_q}{dt} = U_{LO} - \frac{1}{8\pi^3} \int d\mathbf{q} \frac{n_q - n_q^0}{\tau_{LO}}, \quad (4)$$

where U_{LO} is the LO phonon collision operator $\hbar\omega_{LO}U_{LO} = C^E$, n_q is the phonon number, and n_q^0 is the LO phonon occupation number when its temperature $T_{LO} = T_A$.

For simplicity, n_q in Eq. (4) is assumed symmetric in \mathbf{q} -space. To estimate $|\mathbf{q}|_{\max}$ for hot LO phonons, a series of bulk GaN electron drift velocity versus electric field simulations, like those shown in Fig. 3, were conducted. As indicated in Fig. 4, these simulations also computed LO phonon occupation numbers for different ranges of $|\mathbf{q}|$. Based on these data, $|\mathbf{q}|_{\max} = 6 \times 10^6 \text{ 1/cm}$ was used in Eq. (4) for GaN HEMT device simulations.

III. GAN HEMT SETUP AND SIMULATION RESULTS

A. Device Configuration

The device structure is illustrated in Fig. 5. The heterostructure layers were grown by metalorganic chemical vapor deposition (MOCVD) with growth temperatures of various layers

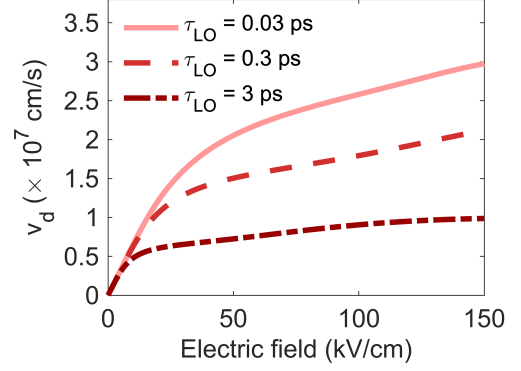


FIG. 3. Bulk electron drift velocity versus field for intrinsic GaN at room temperature for different LO phonon lifetimes.

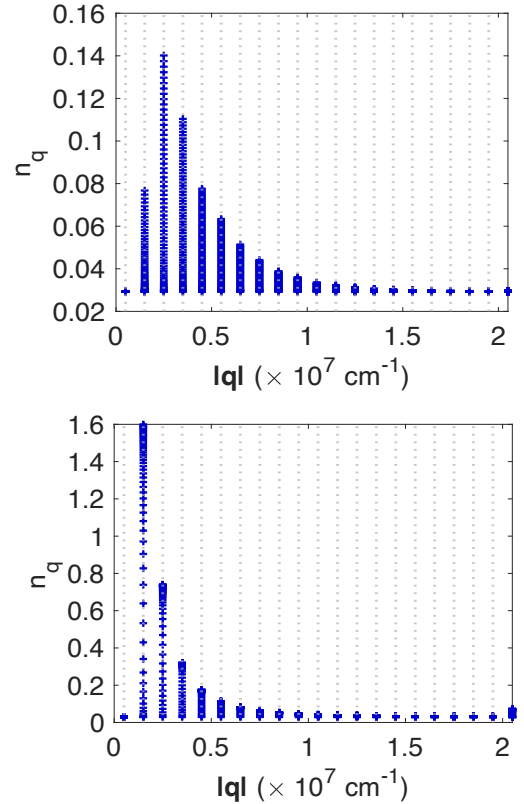


FIG. 4. Occupation numbers n_q for LO phonons emitted into different ranges of phonon momentum $|\mathbf{q}|$ during the simulation of electron drift velocity in bulk GaN. The value of n_q is plotted as a symbol in each range of $|\mathbf{q}|$ for different applied fields, where $|\mathbf{E}|_{\max} = 70 \text{ kV/cm}$ (top) and 600 kV/cm (bottom). $\tau_{LO} = 0.3 \text{ ps}$ was used for each range of $|\mathbf{q}|$.

adjusted to promote good incorporation, defect reduction, and thickness control.²² The device layers are grown on a SiC substrate for improved thermal conduction. A 1 nm $\text{In}_{0.1}\text{Ga}_{0.9}\text{N}$ layer is first grown on GaN buffer on SiC and followed by an 11 nm GaN channel. The top barrier is a 25 nm $\text{Al}_{0.32}\text{Ga}_{0.64}\text{N}$ layer, which is recessed by 12 nm, leading to a 13 nm thick layer underneath the gate contact. The back barrier was shown to promote electron confinement and superior gate modula-

tion efficiency. The gate length is $0.1\ \mu\text{m}$, with source-to-gate (gate-to-drain) spacing of $0.75\ \mu\text{m}$. Additional device-specific parameters are listed in Table I.

The device simulation employs a Dirichlet boundary condition at the bottom of the substrate that holds the lattice temperature equal to 300 K, while a Neumann boundary condition is used at other surfaces. Perfect electric conductors (PECs) on top of the device are treated as iso-thermal bodies.

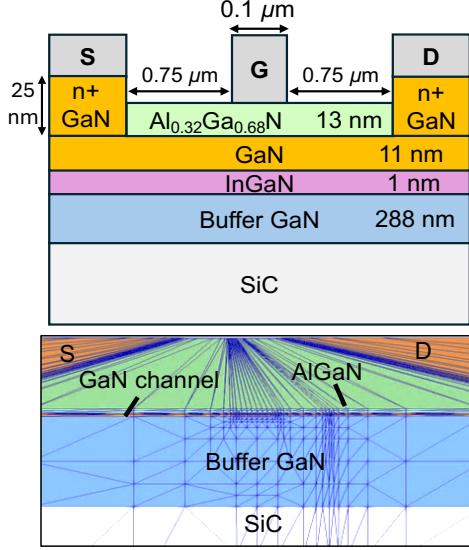


FIG. 5. Cross-section of the fabricated GaN HEMT (top), and the meshed structure (bottom).

TABLE I. Device parameters.

Parameter	Value
Source/Drain doping	$2 \times 10^{19}\ \text{cm}^{-3}$
Gate Schottky barrier height	1.2 eV
Polarization sheet charge density	$1.115 \times 10^{13}\ \text{cm}^{-2}$
Surface trap density (source access)	$1.3 - 3.5 \times 10^{12}\ \text{cm}^{-2}$
Surface trap density (drain access)	$5.2 \times 10^{12}\ \text{cm}^{-2}$
LA/TA phonon deformation potential	8.3 eV
LO phonon deformation potential	$10^9\ \text{eV/cm}$
LO phonon energy	92 meV

B. Device Simulation

Measured and simulated GaN HEMT drain currents I_D versus drain voltage V_{DS} for different gate biases V_{GS} are shown in Fig. 6. The favorable comparison between measured and simulated data indicates that FKT can accurately capture the physics of the fabricated device.²³ The solver predicts that the LO phonon lifetime must be as short as few tens of fs in order to explain the measured I-V characteristics. Specifically, for the results in Fig. 6, $\tau_{LO} = 30\ \text{fs}$. While such a short phonon lifetime may seem unexpected for bulk GaN, it is reasonable in GaN heterostructures, where LO phonon interactions with interfaces create additional decay channels that enable rapid conversion into heat-conducting modes.^{24,25} The impact of

τ_{LO} on the output current at $V_{GS} = 1\ \text{V}$ and $V_{DS} = 10\ \text{V}$ is shown in Fig. 7. As expected, increasing τ_{LO} beyond 30 fs reduces the drain current. Conversely, decreasing τ_{LO} from 30 fs to 1 fs yields a $\sim 30\%$ increase in drain current, indicating that even at ultrashort τ_{LO} the device performance remains constrained by the hot-LO-phonon bottleneck.

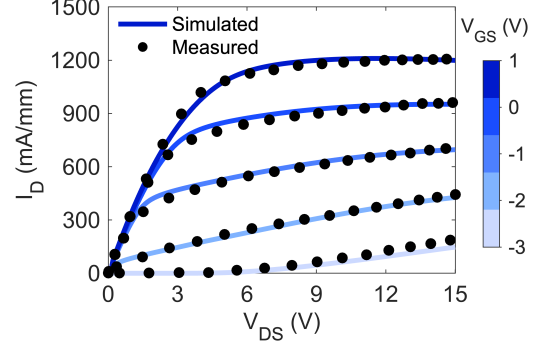


FIG. 6. Simulated output curves with 30 fs hot LO phonon lifetime. Symbols are experimental data from Marino *et al.*²³

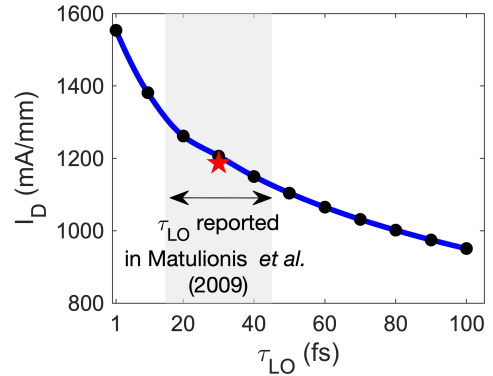


FIG. 7. Degradation of steady-state current at a fixed bias ($V_{GS} = 1\ \text{V}$, $V_{DS} = 10\ \text{V}$) with increasing LO phonon lifetime. The value of τ_{LO} used to compute the currents in Fig. 6 is marked in red.

The role of LO phonon heating is further illustrated in Fig. 8(a), which presents the simulated output characteristics at $V_{GS} = 1\ \text{V}$ under four different conditions. The simulation with $\tau_{LO} = 30\ \text{fs}$ is the baseline result (labeled as “All”), which matches well with the measured data shown in Fig. 6. When LO phonon heating with $\tau_{LO} = 30\ \text{fs}$ is considered but acoustic phonon heating is ignored (result labeled as “LO”), the drain current merely increases by 5% at $V_{GS} = 1\ \text{V}$ and $V_{DS} = 10\ \text{V}$, compared to the baseline case. This observation reinforces that LO phonon heating alone introduces substantial performance degradation even in the absence of acoustic-phonon-induced self-heating. When we assume an instantaneous decay of LO phonons into acoustic modes, effectively removing the hot-LO phonon contribution and considering only longitudinal and transverse acoustic phonon heating (labeled as “LA/TA”), I_D increases by approximately 30% at $V_{GS} = 1\ \text{V}$ and $V_{DS} = 10\ \text{V}$. In contrast, eliminating both hot LO and hot acoustic phonons in the device (labeled as “None”) would increase the device current by up to 50%, suggesting that

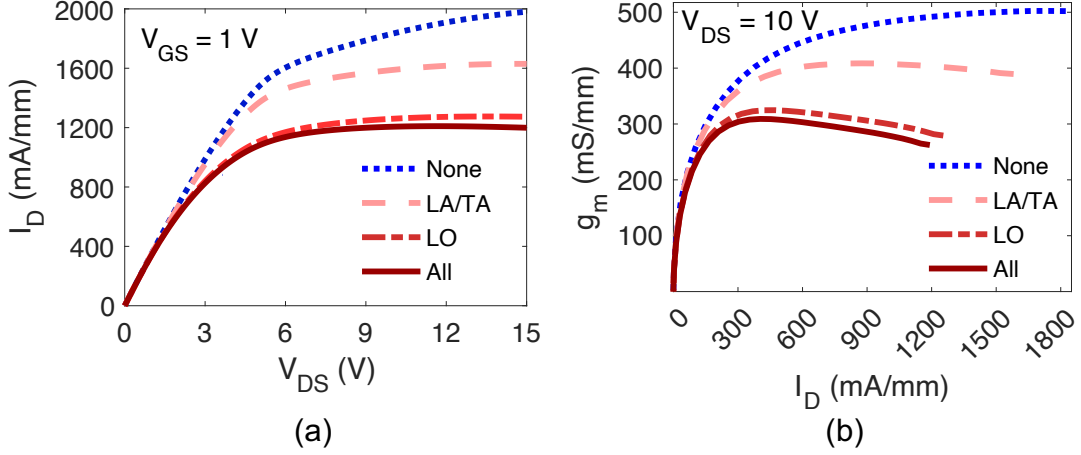


FIG. 8. (a) Simulated steady-state current at a fixed gate bias showing the impact of LO phonon heating. The inclusion of LO phonon heating significantly reduces the current compared to models considering only acoustic phonon heating (LA/TA) or neglecting phonon heating altogether. Even in the absence of acoustic phonon heating, the LO phonon contribution alone is sufficient to notably degrade the output current. (b) Impact of phonon heating on transconductance (g_m) at $V_{DS} = 10$ V.

phonon-engineering strategies could, in principle, enhance intrinsic device performance. However, we are not aware of any studies demonstrating LO-phonon lifetimes below 30 ± 15 fs in GaN heterostructures, indicating that such aggressive lifetime reduction has not yet been realized experimentally.

Similar to the trends observed for I_D , the transconductance, g_m , is also significantly affected by the degree of LO-phonon heating, even when hot phonons decay rapidly into acoustic modes. As shown in Fig. 8(b), the peak g_m would increase by roughly 30% in the absence of LO-phonon heating, and by nearly 60% if all phonon heating were eliminated.

C. Electron and Phonon Temperatures

Examining electron and phonon temperatures within the GaN HEMT may offer insights into the device behaviors presented in Section III B. Figure 9(a) shows the peak phonon temperature in the GaN channel for the simulation configurations corresponding to Fig. 8(a). When only acoustic phonon heating is included, T_A rises uniformly above 300 K due to Joule heating. Since LO phonon heating is not considered in this case, the temperature of optical phonons is the same as that of acoustic phonons. However, when hot-phonon effects are explicitly included with $\tau_{LO} = 30$ fs, a clear decoupling between T_A and T_{LO} emerges. The LO phonon temperature increases sharply with drain bias, exceeding 1800 K at high fields, while the acoustic phonon temperature remains substantially lower. Figure 9(b) further highlights how the assumed heating mechanisms lead to distinct phonon temperature profiles, particularly under the high drain bias where these differences are most pronounced.

We also investigate the spatial profiles of lattice and electron temperatures along the channel length probed directly below the AlGaIn/GaN interface, as shown in Fig. 10(a). Although the lattice heats only up to about 390 K at $V_{GS} = 1$ V and $V_{DS} = 10$ V, the electron temperatures can be as high as 2800 K. Furthermore, we can see that the electron temperature peaks sharply near the gate-drain edge. This region co-

incides with the high electric field in the channel, where carriers gain substantial kinetic energy and predominantly lose it through LO phonon emission. Although the electron temperature is elevated at the gate-drain edge, the carrier density in this pinch-off region is substantially depleted, and this low density of hot electrons traverses the pinch-off region at a high rate compared to the phonon scattering rate. As a result, the number of LO phonons emitted by these hot electrons is moderate, as shown in Fig. 10(b), causing the nonequilibrium LO-phonon occupation number to stay close to its equilibrium value within this narrow depleted region. Just beyond the pinch-off region, however, in the access region, the electron density increases rapidly, and access region electrons heat up by absorbing the energy carried by the nearly ballistic electrons that emerge from the pinch-off region. This results in a much larger population of carriers in the access region capable of emitting LO phonons. This enhanced emission drives the LO-phonon occupation above equilibrium, particularly for longer LO-phonon lifetimes, which increases phonon reabsorption and reduces electron cooling. As a result, we observe larger τ_{LO} values producing elevated electron temperatures in the access regions, despite reduced net emission in the pinch-off region.

The temperature variations in Fig. 10 also reveal certain characteristics of acoustic phonon lattice heating. In contrast to the electron temperature profile, the lattice temperature exhibits a more gradual spatial variation, increasing smoothly along the channel due to the slower energy transfer from electrons to acoustic phonons mediated by LO phonon decay. The lattice temperature's dependence on τ_{LO} also appears to be in contrast to the electron temperature. Under nonequilibrium steady-state conditions, the power supplies inject energy into the device as $V_{DS}I_D$, which first heats the mobile electrons through Joule heating. The hot electrons, in turn, transfer their energy to the LO phonons through scattering, which subsequently decay into acoustic phonons that ultimately diffuse heat into the heat sinks. Increasing the LO phonon life-

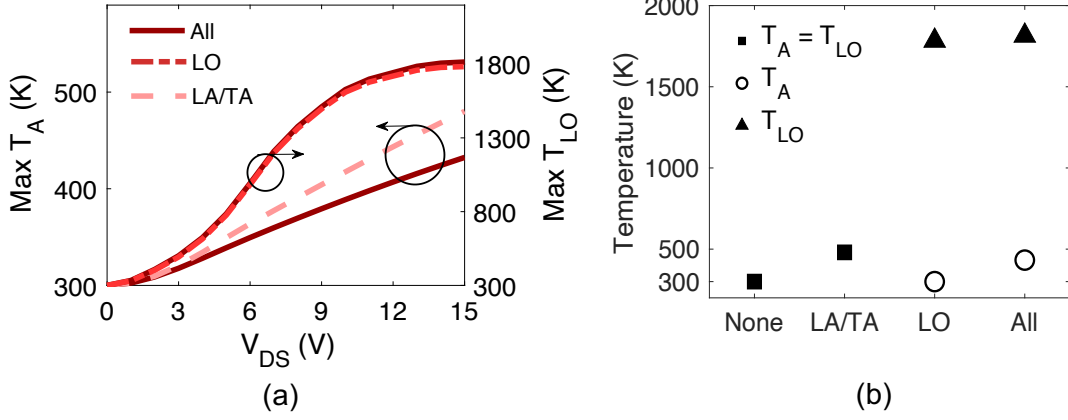


FIG. 9. (a) Gradual rise of peak acoustic phonon temperature and LO phonon temperature in the channel versus V_{DS} at $V_{GS} = 1$ V. (b) Peak acoustic phonon temperature and LO phonon temperature in the channel ($V_{GS} = 1$ V, $V_{DS} = 15$ V). For cases with LO phonon heating, $\tau_{LO} = 30$ fs.

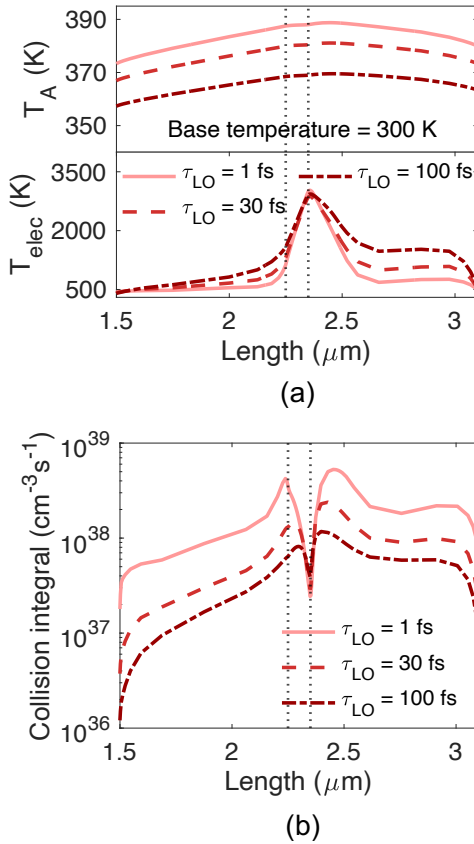


FIG. 10. (a) Acoustic phonon temperature (top) and electron temperature (bottom), and (b) collision integral along the channel length at 0.1 nm below the AlGaIn/GaN interface ($V_{GS} = 1$ V, $V_{DS} = 10$ V). The channel is marked by the dotted vertical lines.

time, τ_{LO} , strengthens the hot-phonon bottleneck where the long-lived LO phonons accumulate in the channel, forming a nonequilibrium population that repeatedly reabsorbs energy from the hot electrons. This elevates T_{LO} , suppresses electron mobility, and reduces the overall current and power dissipation $V_{DS}I_D$. The resulting drop in $V_{DS}I_D$ leads to a lower rate of energy that needs to be carried away by the acoustic phonons,

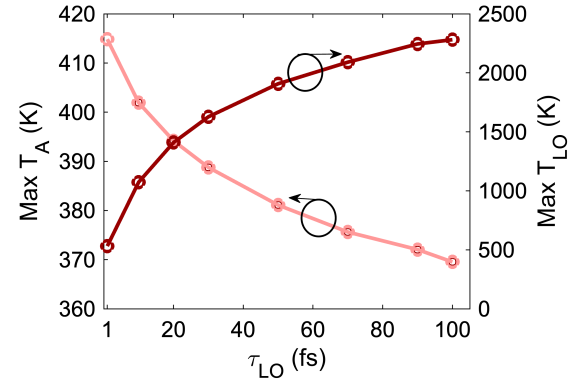


FIG. 11. Peak acoustic phonon temperature and LO phonon temperature in the channel ($V_{GS} = 1$ V, $V_{DS} = 10$ V).

thereby reducing the maximum T_A . This establishes a negative feedback mechanism, where we observe that increased τ_{LO} leads to stronger electron heating but weaker lattice self-heating across the GaN channel. This explains the opposing trends of the peak lattice temperature and LO phonon temperature observed in Fig. 11, where increasing τ_{LO} causes the peak T_{LO} to rise while the peak T_A decreases. Therefore, reduced lattice self-heating with longer phonon lifetime originates not directly from phonon accumulation, but from the diminished Joule heating due to lower electron mobility and current flow.

IV. DISCUSSION

In GaN transistors operating under high electric fields, electron-phonon scatterings can have a significant impact on electron transport. When nonequilibrium LO phonons are generated, they can introduce an additional intrinsic bottleneck that limits performance. Establishing benchmarks for the impact of hot LO phonons on output current and transconductance is therefore critical for understanding whether they significantly hinder further improvements in key HEMT metrics such as cutoff frequency and RF linearity, both of which are closely tied to the device transconductance. Consequently, any degra-

duction of transconductance due to LO phonons directly constrains the RF performance of the device.

The lifetime of hot LO phonons determines the severity of their influence on device behavior. This lifetime arises from a complex interplay of factors, including ambient temperature, carrier density, and supplied power determining electron temperature.^{24,26–29} The lifetime is known to decrease with increasing carrier density due to plasmon–LO phonon coupling, which enhances lattice anharmonicity.³⁰ The resulting coupled phonon–plasmon modes possess higher group velocities, allowing phonons to escape from the active channel region more efficiently. In bulk GaN, the lifetime of the coupled LO-phonon-plasmon mode is several 100s of femtoseconds, while at low carrier densities the LO phonon mode can live for a few picoseconds. In contrast, in AlGaIn/GaN the involved wavevectors in electron-phonon interaction result in Landau damped plasma modes, making quantitative assessment of the lifetime more challenging.^{18,19}

Experimental studies of an AlGaIn/GaN heterostructure by Matulionis *et al.* reported lifetimes of 30 ± 15 ps at supplied powers of 20 ± 10 nW per electron, while Liberis *et al.* observed lifetimes ≤ 50 fs for powers ≥ 10 nW per electron. These results suggest that additional mechanisms in heterostructures can suppress the LO phonon lifetime by nearly two orders of magnitude compared to bulk GaN. It has been proposed that coupled phonon–plasmon modes in heterostructures can propagate toward the interface more rapidly than they decay within the channel, resulting in the observed ultrafast lifetimes. Figure 12 summarizes the range of τ_{LO} values reported in the literature for bulk GaN and AlGaIn/GaN heterostructure.

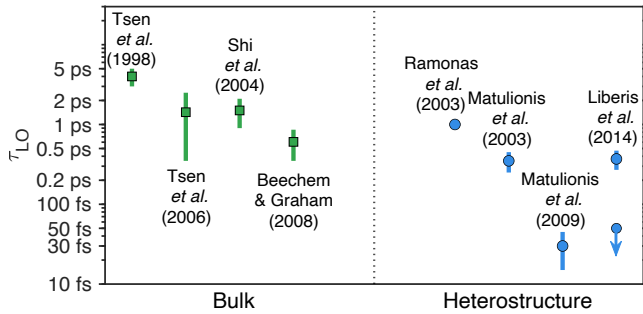


FIG. 12. LO phonon lifetime reported in previous works.^{25–27,31–35}

FKT simulations suggest that only ultrashort LO phonon lifetimes, below 40 fs, can reproduce the measured device characteristics. Longer lifetimes lead to a pronounced hot-phonon bottleneck that contradicts experimental observations. A key question is whether the measured DC characteristics could be reproduced by adjusting other device parameters in a way that would permit longer LO phonon lifetimes (*e.g.*, $\tau_{LO} \sim 100$ fs). While certain device features, such as the surface-state densities in the source and drain access regions, can be varied within physically reasonable ranges and affect the current levels to achieve a reasonable match for τ_{LO} below 40 fs, the realistic variability of other model parameters is rather limited due to the fully physical basis of FKT. De-

vice features such as the Schottky barrier height, polarization sheet charge density, or channel doping are tightly constrained by threshold voltage, contact resistance, and known epitaxial profiles; significant modification of these values leads to unphysical threshold voltages or incorrect subthreshold slopes. Among the device features that can be reasonably modified, none are capable of reproducing the measured I–V characteristics over the entire bias space when τ_{LO} exceeds ~ 40 fs. Our prior simulations further demonstrate that increases in τ_{LO} and other combinations of device features cannot simultaneously yield the near-threshold conduction and high-field current saturation. In contrast, ultrafast LO phonon decay ($\tau_{LO} \lesssim 40$ fs) consistently yields agreement across all operating regions, irrespective of small variations in pertinent device features, *e.g.*, access-region surface traps.

Thus, although uncertainties about measured device features introduce some flexibility in defining the simulated structure, the overarching conclusion remains robust: the measured characteristics of this fabricated HEMT can only be explained when LO-phonon heating is limited by ultra-short phonon lifetimes far below those of bulk GaN. This outcome aligns with prior measurements in GaN heterostructures but represents the first theoretical investigation of LO-phonon lifetimes within a realistic HEMT using a full-band transport solver. The limited and physically constrained degrees of freedom available in the device model prevent long-lived LO phonons from being accommodated, reinforcing the conclusion that LO phonon lifetime must be short in practical GaN HEMTs compared to their bulk structures, yet these shortlived optical phonons can significantly suppress current density and transconductance.

V. CONCLUSIONS

The FKT framework is employed to model hot-phonon effects in AlGaIn/GaN HEMTs, incorporating full-band electronic structure and non-equilibrium LO phonon dynamics. The simulations showed not only that ultrashort LO-phonon lifetimes of $\lesssim 40$ fs are required to reproduce measured DC characteristics, consistent with prior studies on GaN heterostructures, but also that, although the LO-phonon decay is fast, it is still not sufficiently fast to eliminate the hot-phonon bottleneck. As a result, the saturated output current and peak transconductance remain degraded by approximately 30% and 60%, respectively. This study also highlighted the intricate interplay between electron transport, phonon dynamics, and power dissipation, demonstrating how increasing τ_{LO} lowered carrier mobility and drain current, thereby reducing the injected power $V_{DS}I_D$ and the corresponding acoustic phonon heat flow into the sinks. Consequently, the maximum lattice temperature T_A decreased. These findings are significant for elucidating the intrinsic performance limits imposed by phonon dynamics and for guiding material and device engineering strategies aimed at achieving higher output current and transconductance.

ACKNOWLEDGMENTS

This work was supported by AFOSR Grant No. LRIR 24RYCOR009, DARPA Agreement No. HR00112390072,

and NSF Grant No. ECCS-2237663.

AUTHOR DECLARATIONS

Conflict of Interest

The authors have no conflicts to disclose.

Author Contributions

Ankan Ghosh Dastider: Formal analysis (lead); Investigation (equal); Validation (lead); Visualization (lead); Writing original draft (equal). **Matt Grupen:** Conceptualization (equal); Investigation (equal); Software (lead); Methodology (lead); Writing original draft (equal); Resources (equal). **Ashwin Tunga:** Validation (supporting); Visualization (supporting); **Shaloo Rakheja:** Conceptualization (equal); Funding acquisition (lead); Project administration (lead); Resources (equal); Supervision (lead); Writing original draft (equal).

DATA AVAILABILITY STATEMENT

The data that support the findings of this study are available from the corresponding author upon reasonable request.

REFERENCES

- ¹K. Hoo Teo, Y. Zhang, N. Chowdhury, S. Rakheja, R. Ma, Q. Xie, E. Yagyu, K. Yamanaka, K. Li, and T. Palacios, "Emerging GaN technologies for power, RF, digital, and quantum computing applications: Recent advances and prospects," *Journal of Applied Physics* **130** (2021).
- ²H. Lu, M. Zhang, L. Yang, B. Hou, R. P. Martinez, M. Mi, J. Du, L. Deng, M. Wu, S. Chowdhury, *et al.*, "A review of GaN RF devices and power amplifiers for 5G communication applications," *Fundamental Research* **5**, 315–331 (2025).
- ³G. Meneghesso, M. Meneghini, and E. Zanoni, "Breakdown mechanisms in AlGaIn/GaN HEMTs: An overview," *Japanese Journal of Applied Physics* **53**, 100211 (2014).
- ⁴J. Barker, D. Ferry, D. Koleske, and R. Shul, "Bulk GaN and AlGaIn/GaN heterostructure drift velocity measurements and comparison to theoretical models," *Journal of Applied Physics* **97** (2005).
- ⁵O. Ambacher, J. Smart, J. Shealy, N. Weimann, K. Chu, M. Murphy, W. Schaff, L. Eastman, R. Dimitrov, L. Wittmer, *et al.*, "Two-dimensional electron gases induced by spontaneous and piezoelectric polarization charges in N- and Ga-face AlGaIn/GaN heterostructures," *Journal of Applied Physics* **85**, 3222–3233 (1999).
- ⁶J. Khurgin, Y. J. Ding, and D. Jena, "Hot phonon effect on electron velocity saturation in GaN: A second look," *Applied Physics Letters* **91** (2007).
- ⁷G. P. Srivastava, "Origin of the hot phonon effect in group-III nitrides," *Phys. Rev. B* **77**, 155205 (2008).
- ⁸S. Barman and G. P. Srivastava, "Long-wavelength nonequilibrium optical phonon dynamics in cubic and hexagonal semiconductors," *Phys. Rev. B* **69**, 235208 (2004).
- ⁹B. K. Ridley, "The LO phonon lifetime in GaN," *Journal of Physics: Condensed Matter* **8**, L511 (1996).
- ¹⁰B. K. Ridley, W. J. Schaff, and L. F. Eastman, "Hot-phonon-induced velocity saturation in GaN," *Journal of Applied Physics* **96**, 1499–1502 (2004).
- ¹¹B. K. Ridley FRS, "Hot phonons," in *Quantum Processes in Semiconductors* (Oxford University Press, 2013).
- ¹²A. Matulionis, "Hot phonons in GaN channels for HEMTs," *physica status solidi (a)* **203**, 2313–2325 (2006).
- ¹³T. Fang, R. Wang, H. Xing, S. Rajan, and D. Jena, "Effect of Optical Phonon Scattering on the Performance of GaN Transistors," *IEEE Electron Device Letters* **33**, 709–711 (2012).
- ¹⁴M. Grupen, "An alternative treatment of heat flow for charge transport in semiconductor devices," *Journal of Applied Physics* **106**, 123702 (2009).
- ¹⁵M. Grupen, "Energy transport model with full band structure for GaAs electronic devices," *Journal of Computational Electronics* **10**, 271–290 (2011).
- ¹⁶M. Grupen, "GaN high electron mobility transistor simulations with full wave and hot electron effects," *IEEE Transactions on Electron Devices* **63**, 3096–3102 (2016).
- ¹⁷A. Tunga, K. Li, E. White, N. C. Miller, M. Grupen, J. D. Albrecht, and S. Rakheja, "A comparison of a commercial hydrodynamics tcad solver and fermi kinetics transport convergence for GaN HEMTs," *Journal of Applied Physics* **132** (2022).
- ¹⁸B. K. Ridley and A. Dyson, "The Lifetime of Polar-Optical Modes in Semiconductors," *MRS Proceedings* **1221**, 1221–CC06–05 (2009).
- ¹⁹A. Dyson and B. K. Ridley, "The lifetime of optical phonons in a single heterostructure," *Journal of Applied Physics* **109**, 054509 (2011).
- ²⁰N. C. Miller, J. D. Albrecht, and M. Grupen, "Large-signal RF GaN HEMT simulation using Fermi Kinetics Transport," in *2016 74th Annual Device Research Conference (DRC)* (2016) pp. 1–2.
- ²¹S. Sridharan, A. Christensen, A. Venkatachalam, S. Graham, and P. D. Yoder, "Temperature- and Doping-dependent Anisotropic Stationary Electron Velocity in Wurtzite GaN," *IEEE Electron Device Letters* **32**, 1522–1524 (2011).
- ²²T. Palacios, C.-S. Suh, A. Chakraborty, S. Keller, S. DenBaars, and U. Mishra, "High-performance E-mode AlGaIn/GaN HEMTs," *IEEE Electron Device Letters* **27**, 428–430 (2006).
- ²³F. A. Marino, N. Faralli, T. Palacios, D. K. Ferry, S. M. Goodnick, and M. Saraniti, "Effects of Threading Dislocations on AlGaIn/GaN High-Electron Mobility Transistors," *IEEE Transactions on Electron Devices* **57**, 353–360 (2010).
- ²⁴A. Matulionis, J. Liberis, I. Matulionienė, M. Ramonas, and E. Šermukšnis, "Ultrafast Removal of LO-Mode Heat From a GaN-Based Two-Dimensional Channel," *Proceedings of the IEEE* **98**, 1118–1126 (2010).
- ²⁵J. Liberis, M. Ramonas, E. Šermukšnis, P. Sakalas, N. Szabo, M. Schuster, A. Wachowiak, and A. Matulionis, "Hot-phonon lifetime in Al_{0.23}Ga_{0.77}N/GaN channels," *Semiconductor Science and Technology* **29**, 045018 (2014).
- ²⁶K.-T. Tsen, D. Ferry, A. Botchkarev, B. Sverdlov, A. Salvador, and H. Morkoc, "Time-resolved raman studies of the decay of the longitudinal optical phonons in wurtzite GaN," *Applied Physics Letters* **72**, 2132–2134 (1998).
- ²⁷K.-T. Tsen, J. G. Kiang, D. Ferry, and H. Morkoc, "Subpicosecond time-resolved raman studies of LO phonons in GaN: Dependence on photoexcited carrier density," *Applied Physics Letters* **89** (2006).
- ²⁸A. Dyson, "Phonon-plasmon coupled modes in GaN," *Journal of Physics: Condensed Matter* **21**, 174204 (2009).
- ²⁹A. Matulionis and H. Morkoc, "Hot phonons in InAlN/AlN/GaN heterostructure 2DEG channels," in *Gallium Nitride Materials and Devices IV*, Vol. 7216 (SPIE, 2009) pp. 65–78.
- ³⁰A. Dyson and B. K. Ridley, "Phonon-plasmon coupled-mode lifetime in semiconductors," *Journal of Applied Physics* **103**, 114507 (2008).
- ³¹L. Shi, F. A. Ponce, and J. Menéndez, "Raman line shape of the A1 longitudinal optical phonon in GaN," *Applied Physics Letters* **84**, 3471–3473 (2004).
- ³²T. Beechem and S. Graham, "Temperature and doping dependence of phonon lifetimes and decay pathways in GaN," *Journal of Applied Physics* **103**, 093507 (2008).
- ³³M. Ramonas, A. Matulionis, and L. Rota, "Monte carlo simulation of hot-phonon and degeneracy effects in the AlGaIn/GaN two-dimensional electron gas channel," *Semiconductor Science and Technology* **18**, 118 (2003).
- ³⁴A. Matulionis, J. Liberis, I. Matulionienė, M. Ramonas, L. F. Eastman, J. R. Shealy, V. Tilak, and A. Vertiatchikh, "Hot-phonon temperature and lifetime in a biased Al_xGa_{1-x}N/GaN channel estimated from noise analysis," *Phys. Rev. B* **68**, 035338 (2003).
- ³⁵A. Matulionis, J. Liberis, I. Matulionienė, M. Ramonas, E. Šermukšnis, J. H. Leach, M. Wu, X. Ni, X. Li, and H. Morkoc, "Plasmon-enhanced heat dissipation in GaN-based two-dimensional channels," *Applied Physics Letters* **95**, 192102 (2009).